

# Graphene transmembrane nanofluidic devices: fabrication strategies and ion transport Kanq, X.

#### Citation

Kang, X. (2025, November 20). *Graphene transmembrane nanofluidic devices: fabrication strategies and ion transport*. Retrieved from https://hdl.handle.net/1887/4283179

Version: Publisher's Version

Licence agreement concerning inclusion of doctoral

License: thesis in the Institutional Repository of the University

of Leiden

Downloaded from: <a href="https://hdl.handle.net/1887/4283179">https://hdl.handle.net/1887/4283179</a>

**Note:** To cite this publication please use the final published version (if applicable).

# Introduction

#### 1.1 Introduction.

Ion transport is a fundamental process in both biological and technological systems. In nature, biological ion channels exhibit exceptional selectivity, distinguishing ions by their atomic composition and stereochemistry. These channels, which generally self-assemble from polypeptides<sup>1,2</sup>, have complex pore architectures lined with functional groups that enable precise ion selection<sup>3-5</sup>. Inspired by these intelligent natural channels, researchers are developing artificial membranes that mimic these advanced ion transport mechanisms<sup>6-9</sup>.

The development of ion transport technologies has led to significant advancements in various fields. In biomedicine, these technologies enable precise nanoscale drug delivery<sup>10</sup>, ultrasensitive biochemical sensing<sup>11,12</sup>, and integration with microfluidic platforms to allow efficient screening and single-cell resolution analysis<sup>12</sup>. In the energy field, ion transport innovations are improving power generation and storage systems, increasing energy conversion efficiency in fuel cells<sup>13</sup>, enhancing the performance of supercapacitors<sup>14</sup> and advanced batteries<sup>15</sup>, and facilitating novel energy generation methods such as osmotic power from salinity gradients. Additionally, environmental applications include advanced water treatment processes and more efficient seawater desalination, with ion-selective membranes playing a key role in removing contaminants and improving overall efficiency<sup>16-18</sup>.

Here, we first discuss the fundamental principles of ion selectivity transport, focusing on the ion selectivity mechanism, including the selectivity between anions and cations, and among different cations. Synthetic membranes are categorized by their structural dimensionality (e.g., 0D, 2D, or 3D architectures). Graphene is highlighted for its unique monolayer geometry and exceptionally low transmembrane resistance, making it promising for high-efficiency ion transport. However, its dense electronic cloud structure blocks most ions except protons, prompting further investigation into the mechanism of proton-selective transport. Despite its selectivity, the overall proton conductivity remains relatively low, indicating room for improvement. Controllably introducing the defects is a promising way. We therefore describe below various defect types and strategies for introducing them on graphene, emphasizing the controlled engineering of specific defects to enhance both proton conductivity and selectivity.

# 1.1.1 Fundamentals of ion selectivity.

Ion selectivity is a crucial property for ion channels and membranes, referring to the

ability to distinguish between different ions by allowing the specific ions to pass while blocking others. This selectivity is mainly determined by (i) the engineered channel size that imposes steric and hydration energy barriers, (ii) the specific ion-membrane interactions governed by electrostatic and chemical affinity<sup>6,19</sup>.

# 1.1.1.1 Selectivity between ions of different charges.

When a membrane surface is electrically charged, it naturally attracts oppositely charged ions (counter-ions) and repels same-charged ions (co-ions) from the solution, forming an electric double layer (EDL) at the membrane interface<sup>20,21</sup>. The EDL is composed of the Stern layer and the diffusion layer<sup>22,23</sup>. The Stern layer is the region where counter-ions are tightly adsorbed onto the membrane surface. The diffusion layer is the region that extends from the Stern layer to the bulk solution (Figure 1a). Within the diffusion layer, the ion distribution is influenced by both Coulomb forces, which attract counter-ions closer to the membrane surface, and electrostatic screening from the Stern layer, which reduces the membrane surface electrical attraction. As a result, an electric potential is generated on the membrane surface that decays with the distance from the membrane surface into the bulk solution (Figure 1b). The length of this decay is the Debye length (l)<sup>24</sup> and is inversely proportional to the square root of the ionic strength of the electrolyte<sup>25,26</sup>.

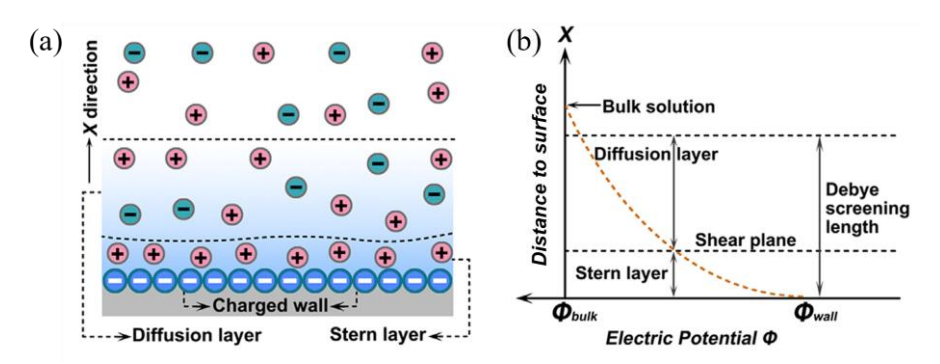


**Figure 1. Structure of EDL and electric potential distribution near a negatively charged surface.** (a) Schematic representation of the EDL structure adjacent to a negatively charged membrane surface, illustrating the Stern layer and the diffuse layer. (b) Electric potential distribution from a negatively charged wall to the bulk solution, showing the non-linear decay of potential across the EDL, with a steep drop in potential within the Stern layer, followed by a gradual decline in the diffuse layer. Adapted from ref<sup>23</sup>.

Ion transport in micro- and nanofluidic channels is influenced by the channel dimensions and the Debye length (l). l ranges from 1 to 100 nm in typical ionic solutions with ionic strengths between 100 mM and 10  $\mu$ M, respectively. In a

microfluidic channel, the channel dimension is much larger than *l*, meaning that the majority of the fluid volume resides in the bulk solution region, beyond the influence of the electric double layer (i.e., outside the Stern and diffuse layers). As a result, both co-ions and counter-ions can move freely through the channel (Figure 2a). In a nanofluidic channel geometry, where the channel size is comparable to *l*, the EDL spans the entire channel volume (Figure 2b). When the channel size is smaller than *l*, counter-ions dominate due to steric exclusion of co-ions at the channel entrance, enabling cation- or anion-selective transport. For example, negatively charged surfaces enhance cation selectivity by enriching mobile counter-ions (*e.g.*, K<sup>+</sup>), while positively charged surfaces favor anion selectivity (*e.g.*, Cl<sup>-</sup>). Additionally, ion selectivity is also influenced by the density of the fixed charge<sup>27</sup>. For example, membranes with low charge density show poor ion selectivity, even though Debye layers overlap.

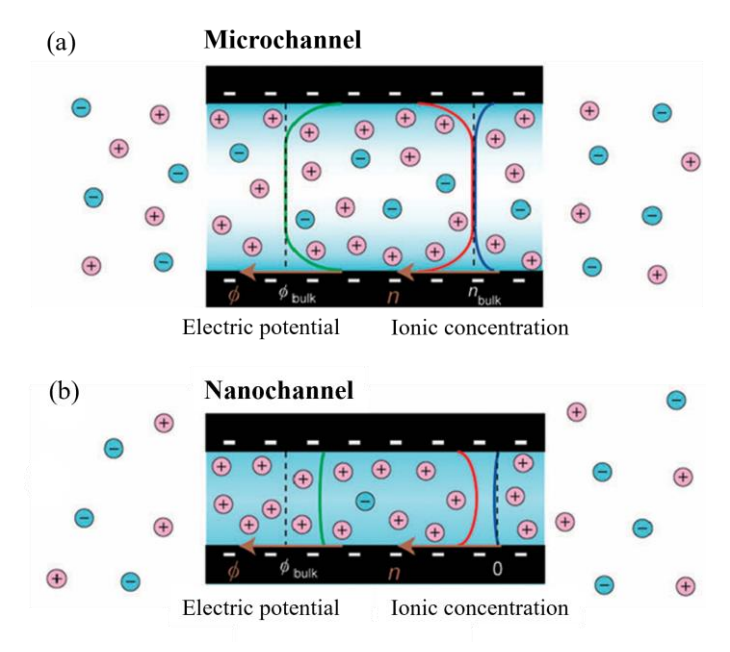


**Figure 2. Effect of channel dimensions on ion selectivity.** (a) In microchannels, where the concentrations of cations (pink) and anions (blue) are equal, both types of ions can freely move through the channel. (b) In nanochannels, the concentration of counter-ions (pink) is higher than co-ions (blue) inside the channel. Adapted from ref<sup>28</sup>.

# 1.1.1.2 Selectivity between ions of the same charge.

In nanochannels containing multiple counter-ion species with the same co-ions, selectivity arises from differences in hydrated ion size and ion-channel affinity. Ions

in aqueous solutions are stabilized by hydration shells, and their effective mobility and interaction with the channel depend critically on their hydrated radius, commonly represented by Stokes radius (r).

When the dimensions of nanochannels are larger than the Stokes radii, ion selectivity is primarily determined by the Stokes radius for ions with the same valence. In this case, smaller Stokes radii correlate with preferential transport, as demonstrated by the selectivity order:  $Ca^{2+} > Mg^{2+}$  and  $K^+ > Na^+ > Li^+$ . For ions with different valences, such as  $Na^+$  and  $Ca^{2+}$ , both their Stokes radius and charges must be considered. Despite its larger Stokes radius,  $Ca^{2+}$  may exhibit stronger permeation due to enhanced electrostatic interactions with charged channel surfaces.

When the dimensions of nanochannels are smaller than the Stokes radius, ion transport undergoes a three-stage process: (1) partial dehydration to shed the hydration shell, (2) translocation through the pore, and (3) rehydration in the bulk solution<sup>29-31</sup>. The thermodynamic stability of hydrated ions, quantified by their standard Gibbs hydration energy ( $\Delta_{hyd}G^{\circ}$ ), which is the energy needed to remove water molecules from the hydration shell and directly governs the energy barrier to dehydration<sup>32</sup>. Ions with stronger hydration (higher  $\Delta_{hyd}G^{\circ}$ ) face higher dehydration barriers, reducing their permeation rates. Figure 3 lists r and  $\Delta_{hyd}G^{\circ}$  values for common cations in aqueous solutions<sup>33,34</sup>.

Ion	Stokes radius (Å)	Gibbs free energies of hydration (kJ mol <sup>-1</sup> )
H <sup>+</sup>	0.28	-1050
$K^+$	1.25	-295
$\mathrm{Ag}^{\scriptscriptstyle +}$	1.48	-430
$Na^+$	1.84	-365
Li <sup>+</sup>	2.38	-475
$Ca^{2+}$	3.10	-1505
$Cu^{2+}$	3.25	-2010
$\mathrm{Mg}^{2+}$	3.47	-1830
$Zn^{2+}$	3.49	-1955
$\mathrm{Fe^{3+}}$	4.06	-4265
Al <sup>3+</sup>	4.39	-4525

**Figure 3.** Stokes radius and standard Gibbs hydration energies of common cations in aqueous solution. The cations are arranged in ascending order of their Stokes radii. Data adapted from

### 1.1.2 Synthetic selective membranes.

Based on these fundamentals, various synthetic membranes have been developed to achieve selective ion transport. Artificial ion-selective channel systems can be categorized into four types based on their pore/channel geometry or ion transport pathways: 3D porous membranes (bulk materials with interconnected pore networks), 2D layered membranes (atomically thin sheets with interlayer nanochannels), 1D nanofluidic channels<sup>23,35</sup> (nanoscale tubular or slit-like geometries), and 0D systems (single nanopore in an atomic membrane).

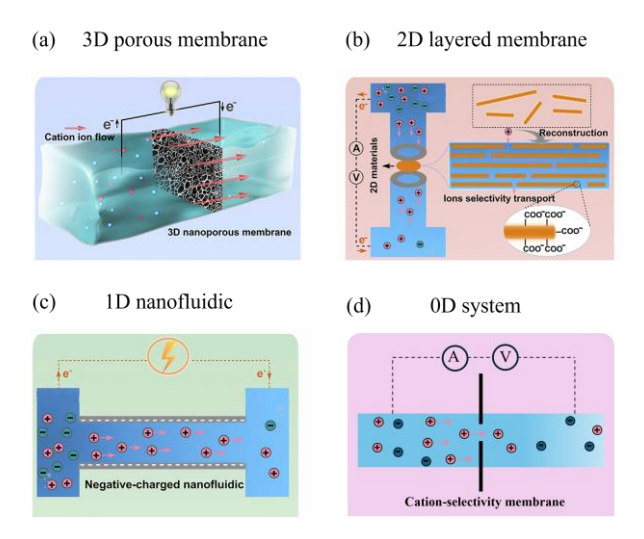


**Figure 4. Nanopore and nanochannel geometries across different dimensions:** (a) 3D porous membrane, adapted from ref<sup>23</sup> (b) 2D layered membrane, adapted from ref<sup>23</sup>. (c) 1D nanofluidic channels, adapted from ref<sup>23</sup>. (d) 0D nanopore system.

# 3D porous membranes:

Ion transport in 3D porous membranes occurs through intricate networks of interconnected pathways, rather than simple linear channels. These complex three-dimensional structures are found in various membrane types, including micrometer-thick polymer films<sup>36,37</sup>, porous carbon/silica films<sup>38,39</sup> and self-assembled nanoparticle-based films. An essential example is Nafion<sup>13</sup>, a sulfonated tetrafluoroethylene copolymer renowned for its proton conductivity.

Nafion consists of a hydrophobic polytetrafluoroethylene (PTFE) backbone that forms a continuous network, and hydrophilic sulfonic acid-terminated side chains (-SO<sub>3</sub>H) which aggregate to create dispersed hydrophilic domains, as illustrated in

Figure 5. The resulting morphology features nanoscale phase separation, where the PTFE matrix provides robust mechanical strength and chemical stability, while the sulfonic acid clusters organize into interconnected hydrophilic channels. These channels absorb water and facilitate proton transport. Upon hydration, the -SO<sub>3</sub>H groups dissociate and release protons (H<sup>+</sup>). These protons interact with water molecules to form hydronium ions (H<sub>3</sub>O<sup>+</sup>), which then move through the ionic network.

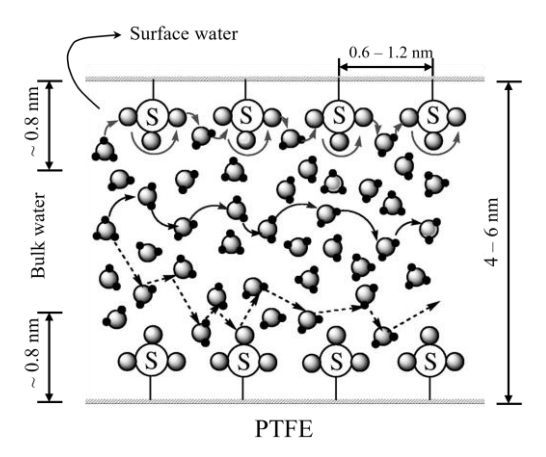


**Figure 5. Schematic of proton transport in fully hydrated Nafion.** The illustration highlights the PTFE backbone and -SO<sub>3</sub>H side chains, and the distribution of water clusters within the Nafion channel, where protons move by hopping between water molecules and -SO<sub>3</sub>H groups via the Grotthuss mechanism. Adapted from ref<sup>40</sup>.

These hydrated protons migrate through the hydrophilic domains *via* two primary conduction mechanisms:

- Grotthuss mechanism<sup>40</sup>: protons move through the hydrogen-bonded water network in the hydrophilic region of Nafion by "hopping" between water molecules and sulfonic acid groups (-SO<sub>3</sub>H). This involves the transfer of a proton from an -SO<sub>3</sub>H group to a nearby water molecule, forming an H<sub>3</sub>O<sup>+</sup> ion. The proton then "hops" again to the next water molecule in the chain, effectively moving through the network by reorganizing hydrogen bonds rather than physically displacing the entire ion. This bond-based transfer is highly efficient, as it avoids the slower process of ions physically diffusing through the membrane. The Grotthuss mechanism dominates in hydrated Nafion membranes, where sufficient water exists to maintain a connected

- pathway for proton hopping.
- Vehicular mechanism<sup>40</sup>: protons are transported by associating with water molecules to form hydrated ions (such as H<sub>3</sub>O<sup>+</sup> or H<sub>5</sub>O<sub>2</sub><sup>+</sup>), which physically move through the water-filled channels in Nafion, carrying the proton with them as they diffuse. This mechanism involves the movement of the hydrated ion itself and is relatively slower compared to the Grotthuss mechanism, but it becomes critical in environments containing a lower water content, particularly in situations where there is not enough water to maintain a continuous hydrogen-bonded network for efficient proton hopping.

In summary, proton transport in Nafion through these two mechanisms is mainly dependent on its hydration state. Sufficient hydration preserves the structural integrity of the hydrophilic domains, maintaining interconnected pathways that enable efficient proton conduction through both the Grotthuss and vehicular mechanisms.

# 2D layered membranes:

These membranes are formed by stacking two-dimensional (2D) materials, such as graphene oxide (GO), transition-metal carbides and nitrides (MXenes), transition-metal dichalcogenides (TMDs), metal-organic frameworks (MOFs), and covalent organic frameworks (COFs). The stacking process typically involves aligning individual 2D sheets, which results in the formation of nanochannels with interlayer spacings of approximately 3–9.5 Å. These nanochannels include:

GO nanosheets<sup>41</sup>, a single-atom-thick layer with lateral dimensions up to tens of micrometers. Their edges and basal planes are featured with oxygen-containing functional groups, including hydroxyl (-OH), carboxyl (-COOH), carbonyl (-C=O), and epoxy (-O-) moieties. When stacked into laminate structures, these nanosheets form 2D nanochannels between interlayers, allowing selective ion transport<sup>42</sup>. By tuning the interlayer spacing with molecular or ionic spacers of controlled size, GO-based membranes can be produced to achieve precise size-selective separation of target ions and molecules from the bulk solution<sup>43</sup>. The interlayer spacing is highly tunable, enabling a broad range of applications<sup>43</sup> (Figure 6a): (1) narrow spacings of 0.3–0.7 nm can be achieved by partially reducing GO, shrinking hydrated functional groups, or by covalently attaching small molecules between sheets, making these structures suitable for desalination processes. (2) Introducing large, rigid chemical moieties or flexible polymer chains, such as polyelectrolytes, can expand the interlayer spacing to 1–2 nm. These configurations are ideal for water purification, wastewater reuse, and the separation of pharmaceuticals and fuels. (3) Inserting

nanoparticles between the layers allows for the expansion of the spacing beyond 2 nm, improving their performance in biomedical applications.

MXenes<sup>44,45</sup>, a family of 2D transition-metal carbides, nitrides, or carbonitrides synthesized by selectively etching the A layer (typically aluminum, gallium, or silicon) from MAX phases ( $M_{n+1}AX_n$ , where M is a transition metal, A is an A-group element, and X is carbon/nitrogen). They can be classified into three structural types:  $M_2X$ ,  $M_3X_2$ , and  $M_4X_3$  (Figure 6b). These materials exist in several forms, including mono-M structures containing a single transition metal, multi-M structures with a mixture of metals, and ordered double-M configurations, where one type of metal occupies the outer layers and another fills the central layer. Their mechanical strength prevents structural degradation, while sharp edges impart antibacterial properties by disrupting bacterial membranes. These features, combined with stable performance in aqueous environments, make MXenes robust for membranes requiring selectivity, durability, and biofouling resistance.

TMDs<sup>46,47</sup>, a layered material with a hexagonal structure, where a metal atom layer (*e.g.*, Mo) is sandwiched between two chalcogen atom layers (*e.g.*, S) (Figure 6c). Among these, molybdenum disulfide (MoS<sub>2</sub>), a typical TMD, features a molybdenum atom layer sandwiched between two sulfur atom layers. Its high surface area and sulfur-rich surfaces provide abundant active sites for ion adsorption and conduction. The inherent electronegativity of sulfur atoms or adsorbed anions imparts a negative charge to MoS<sub>2</sub> nanosheets, favoring selective cation interactions. Adjusting the interlayer spacing optimizes cation transport pathways while creating size exclusion effects that block larger anions, enhancing selectivity. Furthermore, surface functionalization (*e.g.*, with oxygen or nitrogen groups) can tailor the affinity of MoS<sub>2</sub> for specific cations, enabling precise ion-separation applications<sup>48,49</sup>.

MOFs, crystalline porous materials based on metal ions/clusters (nodes) and organic linkers (ligands), with tunable pore size (3–100 Å) and high surface area<sup>50,51</sup> (Figure 6d). Recent advancements in bottom-up synthesis methods have enabled the direct production of ultrathin 2D MOF nanosheets, preserving their porosity and surface functionality while allowing precise control over thickness (sub nm to few nm), pore geometry, and ligand-derived surface chemistry. This tunability makes them ideal materials for ion sieving or gas separation.

COFs, crystalline porous materials formed from organic building blocks linked by strong covalent bonds<sup>52-54</sup> (Figure 6e). Like MOFs, they exhibit tunable pore sizes and high surface areas. The development of surfactant-monolayer-assisted interfacial synthesis (SMAIS) enables the fabrication of free-standing 2D COF membranes with controlled thickness and ordered pore structure, further expanding the potential

applications for selective ion transport, gas separation.

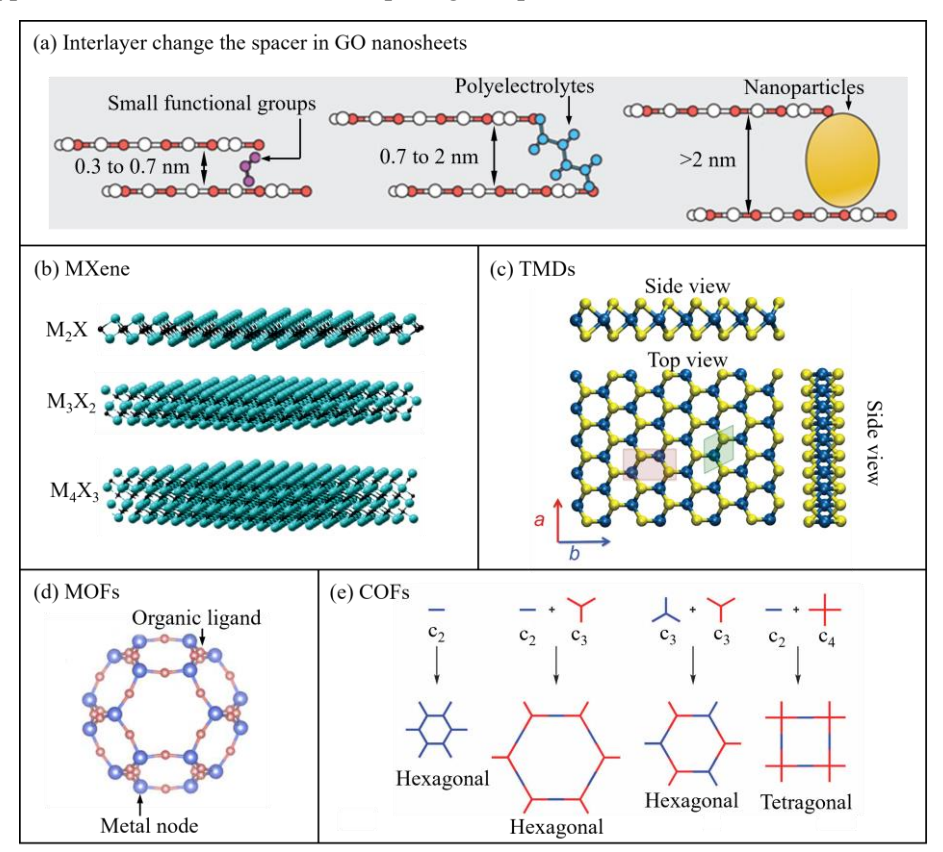


**Figure 6. 2D layered membranes.** (a) GO nanosheets with tunable nanochannel spacing: (1) 0.3-0.7 nm, (2) 1-2 nm. (3) > 2 nm. Adapted from ref<sup>43</sup>. (b) Three structural types of MXenes:  $M_2X$ ,  $M_3X_2$ , and  $M_4X_3$ . Adapted from ref<sup>45</sup>. (c) Atomic structure of TMDs with T = Mo or W. The lattice vectors a and b are illustrated. The hexagonal (green) and rectangular (red) unit cells are marked. Adapted from ref<sup>46</sup>.(d) Schematic of an MOF composed of metal ions and organic ligands that form a porous structure. Adapted from <a href="https://www.nanowerk.com/mof-metal-organic-framework.php">https://www.nanowerk.com/mof-metal-organic-framework.php</a>. (e) Design of 2D COFs by combining building blocks with different geometries. Adapted from ref<sup>54</sup>.

#### 1D nanofluidic channels:

1D nanofluidic channels are characterized by confined pathways where the motion of ions is restricted to a single dominant dimension. These systems feature nanopores or nanochannels with diameters orders of magnitude smaller than their micrometer-scale lengths, creating strong nanoconfinement effects (typically < 10 nm). Key examples include:

Nanotubes, such as carbon nanotubes<sup>55-57</sup> and boron nitride nanotube<sup>58</sup>, are cylindrical nanostructures that enable efficient ion transport due to their atomic-scale smoothness, tunable diameters, and surface charge effects. An example is a single-walled carbon nanotube that contains a hydrogen-bonding network, leading to water molecular motion along the tube axis (Figure 7a).

Nanochannels<sup>59</sup>, engineered nanoscale channels and angstrom-scale slits<sup>60,61</sup> (*e.g.*, graphene gaps), provide precise control over ion selectivity through geometric confinement. A typical angstrom-scale slit consists of three elements: a top flake, a bottom flake, and a spacer (Figure 7b). Together, these components form a channel with walls defined at the atomic level, achieving a thickness of just two atoms. This ultra-confined geometry enables highly selective ion transport by closely matching the dimensions of hydrated ions or molecular species.

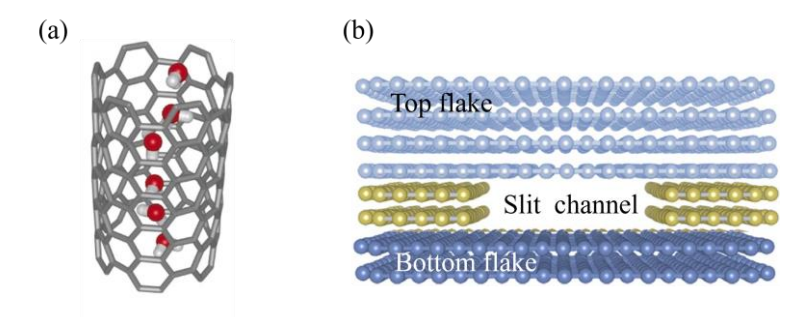


**Figure 7. Typical 1D nanofluidic systems.** (a) Single-walled carbon nanotube. Adapted from ref<sup>55</sup>. (b) Schematic representation of Angstrom-scale slits. Adapted from ref<sup>61</sup>.

# 0D systems:

0D membranes typically refer to the materials where the dimensions of length, width, and height are confined to the nanometer scale. These materials often feature nanoscale pores<sup>62</sup>, such as nanopores created in ultra-thin polymer films or two-dimensional materials (*e.g.*, graphene). Graphene-based 0D membranes are particularly promising due to their atomic-scale thickness, which minimizes transmembrane resistance while enabling exceptional ion selectivity through atomic-scale pore control.

# 1.2 Graphene.

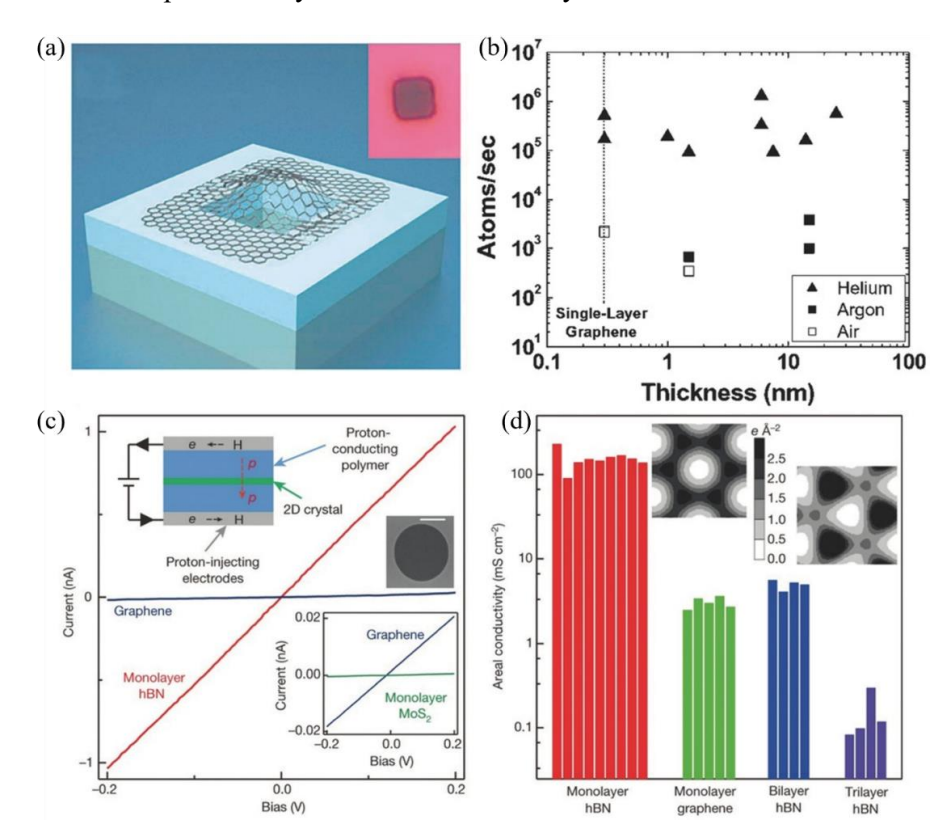
Graphene, a single layer of sp<sup>2</sup> hybridized carbon atoms arranged in a hexagonal lattice, has emerged as an ideal platform for developing ultra-thin molecular separation membranes<sup>63-67</sup>, because of its atomic-scale thickness<sup>68</sup>, exceptional mechanical strength<sup>69</sup>, and a unique electronic cloud structure.

# 1.2.1 Barrier properties of graphene.

Defect-free graphene has been studied as a near-ideal impermeable barrier due to its dense  $\pi$ -electron cloud and lack of intrinsic pathways for molecular transport. In 2008, Bunch *et al*<sup>70</sup>. experimentally validated this property using microchambers sealed with mechanically exfoliated graphene<sup>70</sup>. These chambers were subjected to various gases, including air, argon, and helium, with pressure changes monitored *via* atomic force microscopy (AFM) capable of detecting angstrom-scale graphene surface bulging (Figure 8a). This bulge would alter if gas molecules entered or exited the chamber. Remarkably, even monolayer graphene exhibited complete impermeability to all tested gases, including the smallest gas molecule: helium, with no measurable dependence on membrane thickness (1–75 layers) (Figure 8b).

This experimental observation sparked intense interest in the theoretical understanding of the barrier properties of graphene. Molecular dynamics (MD) simulations and density functional theory (DFT) calculations have quantified the energy barrier for atomic hydrogen and proton permeation through defect-free graphene membranes. Computational models predict high energy barriers for atomic species  $^{69,71,72}$ : above 3 eV for hydrogen  $^{69}$ , oxygen  $^{72}$ , nitrogen  $^{72}$  and helium; and proton (H<sup>+</sup>)  $\geq$  1.2 eV for protons  $^{69}$ . These theoretical calculations align well with the experimental observations, confirming the impermeability of graphene when the atomic lattice is free of defects.

However, in 2014, Hu et al. 73 used a defect-free (mechanically exfoliated) monolayer graphene, sandwiched between two layers of the proton conductor (Nafion) and then connected to proton-injecting electrodes (Figure 8c). By performing DC currentvoltage (I-V) measurements, they determined that the areal proton conductivity of monolayer graphene was 5 mS cm<sup>-2</sup> at room temperature. This study revealed that, despite the dense electron cloud of graphene, protons could tunnel through the vacancies within the cloud (Figure 8d). Proton conductivity can also be measured in other 2D materials, such as hexagonal boron nitride (hBN) and molybdenum disulfide (MoS<sub>2</sub>) (Figure 8c). The differences in conductivity between hBN and graphene were attributed to the different sizes of their electron cloud vacancies (Figure 8d). Graphene has denser and smaller vacancies, which result in lower proton conductivity. This highlighted that the electron cloud vacancies govern the activation energy barrier for proton transport. And then this energy barrier (E) was quantified using Arrhenius-type behavior:  $\sigma \propto exp(-E/k_BT)$ , where  $\sigma$  is the measured proton conductivity at different temperatures (T). An activation energy of approximately 0.78 eV was calculated for proton transport through graphene, which is lower than



the 1.2-2.2 eV predicted by ab initio molecular dynamics simulations.

Figure 8. Experimental setups and results for molecular transport of protons through graphene, hexagonal boron nitride, and molybdenum disulfide. (a) Schematic of a silicon dioxide microchamber sealed by graphene. The insets show the optical image of a suspended monolayer graphene drumhead on a microchamber. (b) Gas transport as a function of the thickness of graphene for all the devices. Adapted from ref<sup>70</sup>. (c) *I-V* curves of monolayer 2D materials – graphene, hBN, and  $MoS_2$  – measured in a proton medium environment. The insets show the illustration of the experimental set-up, an SEM image of the suspended graphene area (scale bar: 1 µm), and the magnified *I-V* curves. (d) Areal proton conductivity of monolayer graphene and mono-, bi-, and trilayer hBN. The insets show the charge densities of monolayer graphene (left) and monolayer hBN (right). Adapted from ref<sup>73</sup>.

# 1.2.2 Proton transport mechanisms across graphene.

#### 1.2.2.1 Atomic-scale defects.

A proposed explanation is that atomic-scale defects in graphene promote proton transport (Figure 9a)<sup>74</sup>. This explanation is primarily relevant for chemical vapor deposition (CVD)-grown graphene, which inevitably introduces defects, such as

grain boundaries, intrinsic sub-nanometer defects, wrinkles, etc., into the lattice. Achtyl *et al.*<sup>74</sup> experimentally demonstrated that protons can transport across graphene *via* nanoholes in the lattice, which are usually considered as defect sites. Through density functional theory (DFT) and reactive force field (ReaxFF) molecular dynamics simulations, it was shown that hydroxyl-terminated atomic-scale defects facilitate proton transfer with a remarkably low energy barrier of approximately 0.61 eV for aqueous proton transport across the graphene membrane.

Additionally, Stone-Wales defects<sup>75</sup>, characterized by adjacent 5- and 7-membered carbon rings (55-77 defects), can occur in both CVD and mechanically exfoliated graphene. An *et al.*<sup>76</sup> found that proton transport through 7-membered rings is 10<sup>6</sup> times higher than through 6-membered rings. This suggests that even a low concentration (~1 ppm) of 7-membered ring defects can still dominate the transport process. Griffin *et al.*<sup>77</sup> further supported this finding by experimentally reporting proton conductivities of ~2 S cm<sup>-2</sup> in graphene enriched with 7- and 8-membered rings – nearly 1000 times higher than in defect-free graphene, when using graphene with a high density of 7 and 8-membered rings. However, such extended non-hexagonal ring configurations are uncommon in standard CVD or exfoliated graphene.

Remarkably, in 2022, Bentley *et al.*<sup>78</sup> employed scanning electrochemical cell microscopy (SECCM)<sup>79,80</sup> to spatially resolve proton transport across CVD graphene. SECCM is a pipette-based imaging technique that combines electrochemical current mapping and surface topographical characterization with microscopic resolution, enabling direct correlation between structural features (*e.g.*, defects) and electrochemical activity. In this study, proton conduction in CVD graphene occurs almost exclusively at localized macroscopic defects – such as cracks, holes, or grain boundaries – with active areas as small as ~0.003 mm². Importantly, > 99% of the graphene surface exhibited no measurable proton permeability, demonstrating that defect-free regions remain impermeable even under electrochemical bias.

# 1.2.2.2 Hydrogenation mechanism.

Another proposed explanation for proton transport through graphene involves hydrogenation-induced structural modifications (Figure 9b)<sup>81,82</sup>. When graphene is exposed to hydrated Nafion or HCl solution, a proton is chemically adsorbed onto graphene, forming a C-H bond. A very high energy barrier of approximately 3.5 eV needs to be overcome for proton flip from one side to the other side<sup>69,83,84</sup>. However, instead of protons covalently bonding to graphene, if protons first occupy a physisorption state, the barriers are lowered to 1.4~2.6 eV<sup>83,84</sup>. Though still higher

than the experimentally calculated 0.78 eV reported by Hu et al<sup>73</sup>.

Feng *et al.* further demonstrated using *ab initio* path-integral molecular dynamics (PIMD) simulations that nuclear quantum effects reduce the penetration barrier by 0.46 eV (12%). When combined with hydrogenation-induced sp³-bonded carbon atoms, the effective barrier is significantly lowered to < 1 eV, enabling proton permeation under ambient conditions<sup>82</sup>.

Proton transport across graphene can also be described by another mechanism known as adsorption-penetration. The process involves two steps: (1) first, the proton transfers from the aqueous medium to the graphene surface forming a chemisorbed state on the graphene lattice; this is then followed by (2) a "flipping" process, where the chemisorbed proton traverses the lattice to a symmetrically equivalent site on the opposite side of the graphene layer. Feng's work showed that the energy barrier for proton adsorption (step 1) is unlikely to occur under ambient conditions<sup>82</sup>. However, the chemisorbed state is highly stable, resulting in an extremely high barrier for proton flipping (step 2). Bartolomei *et al.* demonstrated that when two protons are covalently bound to a benzene ring, the permeation barrier then reduces to 1.0 eV <sup>81</sup>.

This adsorption-penetration mechanism was confirmed experimentally by Tong *et al.* in 2024<sup>85</sup>. They applied an electric field to a graphene sample through a double-gate, varying the strength of the electric field by changing voltages to precisely control the hydrogenation degree of the graphene. By measuring the proton conductance *in situ*, this study demonstrated that the hydrogenation of graphene indeed increased the transmembrane transport of protons.

#### 1.2.2.3 Nanoscale wrinkles.

Recent research has revealed that nanoscale wrinkles on the graphene surface significantly enhance proton permeability. Hidalgo *et al.*<sup>86</sup> employed SECCM to spatially resolve transport across graphene (Figure 9c). Their experimental design employed mechanically exfoliated graphene suspended over micrometer-sized holes in SiNx substrates. The graphene membrane is attached to a Nafion film (proton conductor) and a Pt electrode (proton collector), forming a closed proton transport pathway (Figure 9d). A dual-channel nanopipette filled with HCl served as the proton source. In such a design, protons can transport from the nanopipette through graphene to the Pt electrode, where the hydrogen evolution reaction (HER) occurs. This reaction converts the proton flux into a measurable current. SECCM-generated current intensity maps revealed localized proton transport hotspots at wrinkle sites, with negligible permeability in intact flat regions. Importantly, the graphene used in this study is defect-free (mechanically exfoliated) graphene, indicating that the

observed proton current was not induced by structural defects. Figure 9e shows the current map of proton transport and the corresponding graphene morphology, characterized by atomic force microscopy (AFM). We can see that a higher proton current is measured in the wrinkles (nanoripples) and near the edges of the hole. These regions share a common feature: graphene experiences significant strain there.

The authors further explained the mechanism of the enhanced proton permeability in the strained area through theoretical calculations. It is known that vacancies in the electron cloud govern proton transport in graphene. Strained regions, such as nanorippled areas, exhibit a lower electron cloud density compared to unstrained regions, thereby facilitating proton transport. In addition, by correlating SECCM proton current maps with AFM topographical data (Figure 9e), the study demonstrated that the nanoripple geometry – particularly the higher-stained regions – correlates with proton conduction hotspots. These results concluded that mechanical strain – rather than atomic scale defects – governs proton permeability in defect-free graphene, providing a paradigm shift in understanding proton transport across graphene.

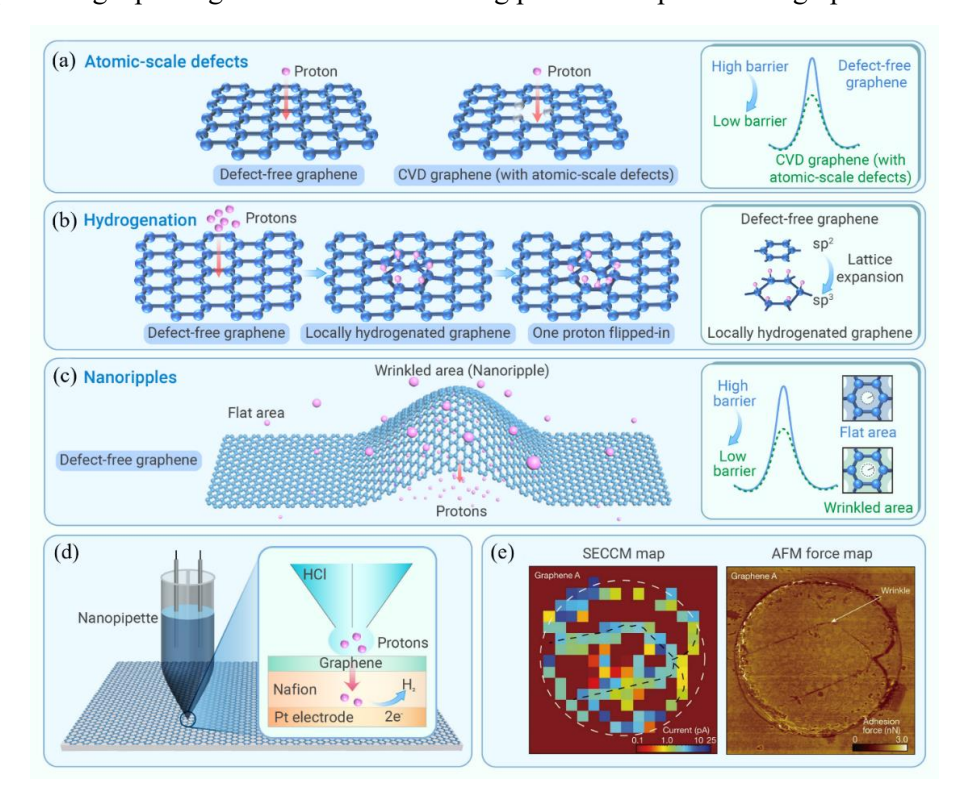


Figure 9. Mechanisms of proton permeation through graphene (a-c) and measurement of proton permeability using scanning electrochemical cell microscope (SECCM, d and

**e).** (a) Illustration showing that protons face a high energy barrier when passing through defect-free graphene, while atomic-scale defects in CVD graphene reduce this barrier. Adapted from ref<sup>74</sup>. (b) In a hydrogenation mechanism, protons chemically bind to graphene, locally altering its structure and allowing them to flip through to the other side. (c) Wrinkles or nanoripples in graphene lower the proton permeation barrier due to reduced electron density in these regions. (d) Schematic of the setup for measuring the proton transport through graphene using SECCM. (e) SECCM current map and corresponding AFM force map for graphene suspended on a Nafion film. Adapted from ref<sup>87</sup>.

#### 1.2.3 Structural defects on graphene.

As mentioned above, atomic defects, hydrogenated graphene, and wrinkles significantly influence proton transport across graphene. These results inspire the exploration of controlled defect engineering to enhance the transmembrane conductivity of protons and other ions. To begin, it is important to understand the types of defects and their respective roles. In graphene, defects are generally classified into several categories: Stone-Wales defect, vacancies, adatoms, substitutions, dislocations, and grain boundaries<sup>75,88</sup>.

#### Stone-Wales defect.

A Stone-Wales defect in graphene is formed by a 90° rotation of a C-C bond, which reconstructs four adjacent hexagons into a non-hexagonal arrangement consisting of two pentagons and two heptagons<sup>89</sup>. This transformation preserves the total number of carbon atoms, distinguishing it from vacancy or adatom-related defects. The resulting structure, known as the '5-7-7-5' defect, is depicted in Figure 10a.

#### Vacancies.

A vacancy defect occurs when one or a few carbon atoms are missing from the graphene lattice<sup>90,91</sup>. The simplest case, a single vacancy, involves the removal of a single carbon atom, resulting in three dangling bonds. These dangling bonds typically reconstruct into a 5-membered and a 9-membered ring. More complex configurations, such as double or multiple vacancies, according to the number of missing carbon atoms from the graphene lattice, are shown in Figure 10b.

#### Adatoms.

Adatoms are added to the foreign atoms or additional carbon atoms onto the graphene lattice through sp<sup>3</sup> hybridization, as shown in Figure 10c. The bonding strength of these adatoms determines their adsorption mechanism: weaker van der Waals interactions result in physisorption, while stronger covalent bonding leads to chemisorption.

#### Substitutions.

Substitutional doping introduces foreign atoms into the graphene lattice by replacing one or more carbon atoms, as shown in Figure 10d. Common dopants such as boron (B) and nitrogen (N) are particularly effective due to their comparable atomic radius to carbon and their ability to donate or accept electrons.

#### Dislocations.

Dislocations are one-dimensional defects that form tilt boundaries between crystallographic domains with misoriented lattices, where the tilt axis remains normal to the graphene plane<sup>92</sup>. These defects can form through the reconstruction of vacancy chains along either the armchair or zigzag crystallographic direction<sup>93</sup>. For instance, such a defect might consist of an alternating line of pentagon pairs separated by octagons (Figure 10e).

#### Grain boundaries.

During CVD growth, graphene nucleates at multiple points on the metal substrate surface<sup>94</sup>. As the growth progresses, these nucleation sites expand with varying crystallographic orientations, inherently leading to polycrystallinity in the resulting graphene sheet. When these growing domains meet, they merge, forming line defects known as grain boundaries at their interfaces<sup>95</sup>, as illustrated in Figure 10f. These grain boundaries consist of carbon atom rings that are not like the typical six-carbon atom rings, often showing pentagonal, heptagonal, or other non-hexagonal structures<sup>96</sup>.

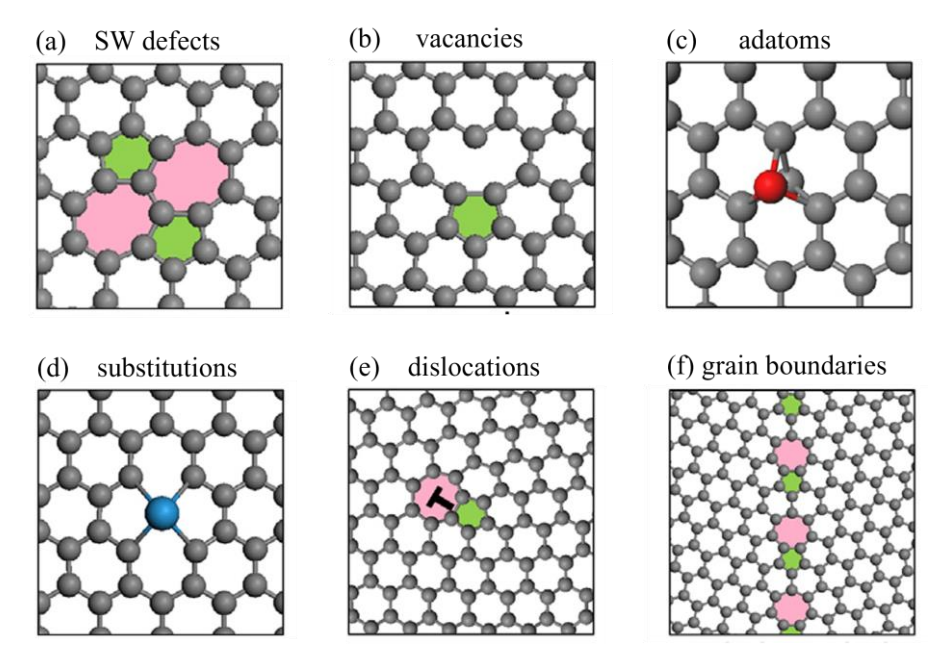


**Figure 10. Schematic of the defect in graphene.** (a) Stone-Wales defects, (b) vacancies, (c) adatoms, (d) substitutions, (e) edge dislocations, and (f) grain boundaries. Adapted from ref<sup>88</sup>.

# 1.2.4 Creating defects on graphene to enhance the ion transport.

The dense  $\pi$ -electron cloud in graphene creates a high-energy barrier for proton transport, resulting in low permeability. However, most simulation studies predict that introducing nanoscale porosity significantly enhances proton conductivity across graphene. This theoretical framework has motivated extensive research into defect engineering strategies aiming at controlling the formation of defects and tuning the size and density of defects.

# 1.2.4.1 Graphene growth.

The CVD process inherently produces various defects in graphene. As mentioned above, grain boundaries occur frequently due to the polycrystallinity of CVD graphene (Figure 11a)<sup>97-99</sup>. Recent advances in precursor design show that a controlled synthesis using polyaromatic hydrocarbons can deliberately create graphene with a disordered structure containing pentagons, heptagons, and distorted hexagons, deviating from the ideal sp<sup>2</sup>-hybridized network (Figure 11b)<sup>100</sup>. Furthermore, heteroatoms (*e.g.*, nitrogen<sup>101</sup>, boron, or sulphur) can be deliberately incorporated into the graphene lattice during the growth process (Figure 11c)<sup>102</sup>. These dopants occupy either substitutional or interstitial lattice sites, altering their

electron cloud structure. More recently, cascaded compression has been introduced as a method to precisely control nanopore formation during graphene growth. This approach involves repeating cycles in which nanopores are first compressed to shrink their size, then expanded in a controlled way. Through these cycles, the pore size and distribution can be gradually adjusted (Figure 11d)<sup>103</sup>.

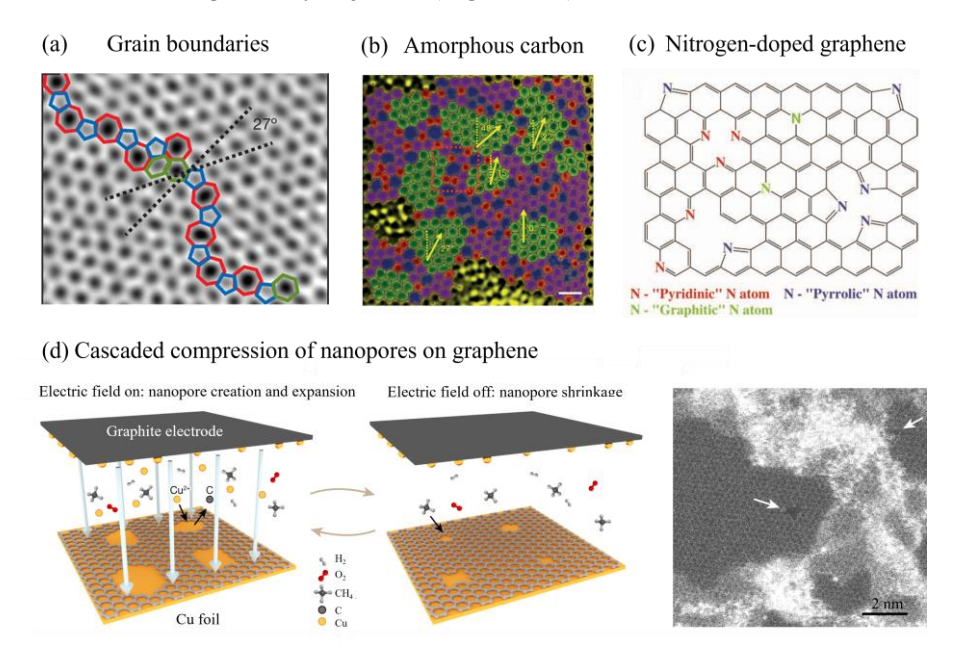


**Figure 11. Defects introduced during CVD synthesis of graphene.** (a) High-resolution transmission electron microscopy (HRTEM) image of a graphene grain boundary. Highlighted atomic structures: pentagons (blue), heptagons (red), and distorted hexagons (green) show the interface between differently oriented graphene domains. Adapted from ref<sup>95</sup>. (b) Colored-enhanced HRTEM image of monolayer amorphous carbon with pentagons (red), heptagons/octagons (blue), and strained hexagons (purple for individual hexagons, green for larger crystallite regions). Adapted from ref<sup>100</sup>. (c) Schematic structure of nitrogendoped graphene. Adapted from ref<sup>101</sup>. (d) *In situ* copper sputtering induces the formation and expansion of nanopores, and a high-resolution STEM image demonstrates precise control over pore size and distribution. Adapted from ref<sup>103</sup>.

#### 1.2.4.2 Particle irradiation.

Particle irradiation offers a targeted approach for introducing defects in graphene. Electron irradiation<sup>104-106</sup> and heavy ion bombardment<sup>107-109</sup> can generate point defects by removing carbon atoms from the lattice. Russo *et al.*<sup>110</sup> demonstrated a method for creating sub-nanometre pores in graphene by selectively removing carbon atoms using 3 keV argon ion bombardment (see Figure 12a). This method

allows control of the pore location, as the argon beam can be directed to specific areas on the graphene sheet. However, it lacks precise control over pore size. To address this limitation, O'Hern *et al.*<sup>111</sup> developed a two-step gallium ion irradiation and chemical etching process (Figure 12b), demonstrating that etching duration directly governs pore size and, consequently, ion selectivity. Despite these advancements, both methods are characterized by relatively slow production rates. The sequential nature of pore creation limits their scalability for applications requiring high pore densities over large areas.

Additionally, using reactive plasma species (Figures 12c-d) has emerged as a scalable alternative for simultaneous structural and chemical modification<sup>112,113</sup>. This technique can introduce various functional groups, potentially enhancing the hydrophilicity of graphene and its proton affinity.

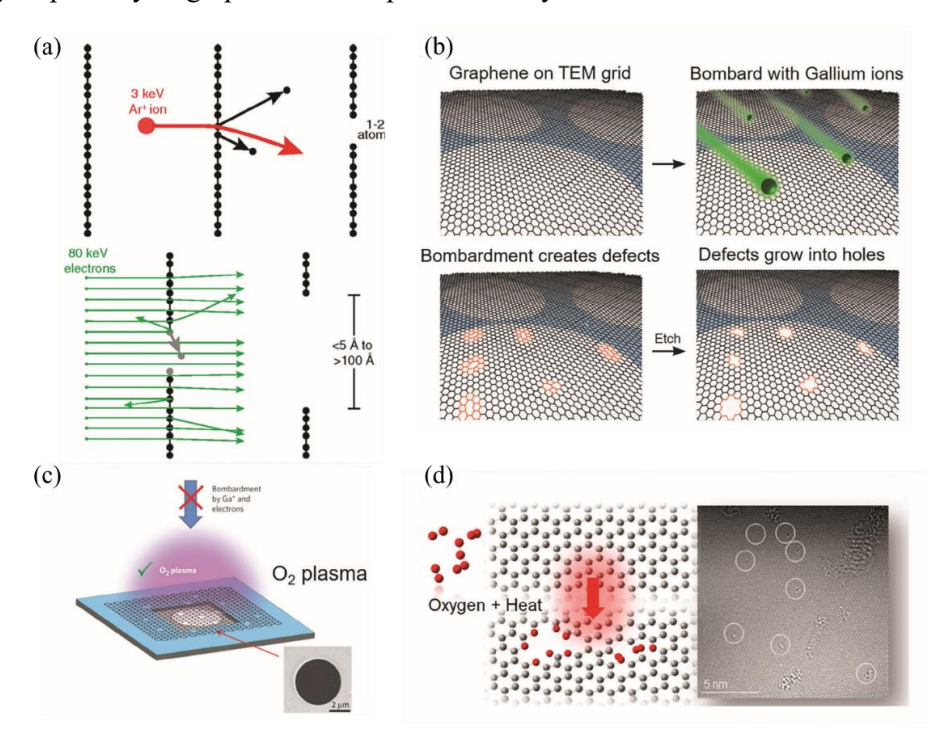


**Figure 12.** (a) Schematic representation of the fabrication process for graphene nanopores using argon ion bombardment and electron beam treatment. Adapted from ref<sup>110</sup>. (b) Illustration depicting the creation of precisely controlled nanopores in graphene achieved by ion bombardment and followed by chemical oxidation treatment. Adapted from ref<sup>111</sup>. (c) Diagram showcasing oxygen plasma etching used to make nanopores in suspended graphene on a silicon microchip, and the SEM image of suspended graphene over the 5  $\mu$ m diameter hole. Adapted from ref<sup>62</sup>. (d) Illustration depicting the introduction of sub-nanometer

vacancy defects in graphene through oxygen gas etching. Adapted from ref<sup>114</sup>.

#### 1.2.4.3 Chemical functionalization methods.

Electrochemical etching of graphene 115,116 enables defect generation in graphene by applying an electrical potential to graphene within an electrolyte solution (Figure 13a). This process drives site-selective oxidation and etching of carbon atoms, creating nanopores. The defect morphology and density can be systematically controlled by optimizing three key parameters: (i) the applied voltage, which dictates the thermodynamic driving force for oxidation reactions; (ii) the electrolyte composition (e.g., pH, ionic species), which modulates reaction kinetics and selectivity; and (iii) the etching duration, which governs defect size evolution and spatial distribution. This etching technologies face limitations in simultaneously satisfying three essential criteria for practical applications: (i) accurate pore size control, (ii) narrow pore distribution, and (iii) high pore density. These requirements are crucial for optimizing the trade-off between selectivity and permeability in molecular/ion separation processes, particularly for proton transport applications. For instance, sub-nanometer pores with narrow size distributions are required to exploit quantum tunneling effects or size exclusion mechanisms, while high pore densities are necessary to ensure sufficient ionic flux.

To address these limitations and further tailor the transport properties of graphene, covalent and non-covalent chemical functionalization have been explored:

The non-covalent functionalization approach utilizes weak interactions such as  $\pi$ - $\pi$  stacking<sup>117</sup>, van der Waals forces, or electrostatic interactions to modify the surface of graphene without disrupting its sp<sup>2</sup>-hybridized lattice. Molecules such as conjugated polymers, surfactants, or polyaromatic hydrocarbons physisorb onto the graphene basal plane, introducing functional groups with different affinities for specific molecules or ions, including protons.

The covalent functionalization uses highly reactive intermediates, such as radicals, nitrenes, carbenes, and arynes, to form strong C-C bonds with the graphene lattice<sup>118</sup>. Diazonium salt-mediated functionalization of graphene exploits electron transfer from the π-electron cloud to aryl diazonium salts<sup>119</sup>, generating reactive aryl radicals that covalently bond to the graphene basal plane. This results in precise control of the functionalization density and spatial distribution, keeping the graphene honeycomb structure largely intact while adding sp<sup>3</sup> carbon atoms that can serve as active sites for proton transport or other reactions. Furthermore, diazonium salts can be designed with different head groups (*e.g.*, sulfonic acid (-SO<sub>3</sub>H), amine (-NH<sub>2</sub>), or carboxyl (-COOH)) to tune the hydrophilicity, charge polarity, or specific

chemical binding. The covalent attachment of functional groups also changes the electron density, enabling precise modulation of its electronic properties (e.g., p/n-type doping). Consequently, the diazonium strategy not only preserves the intrinsic properties of graphene but also facilitates targeted modifications that can tailor its electronic behavior for diverse applications.

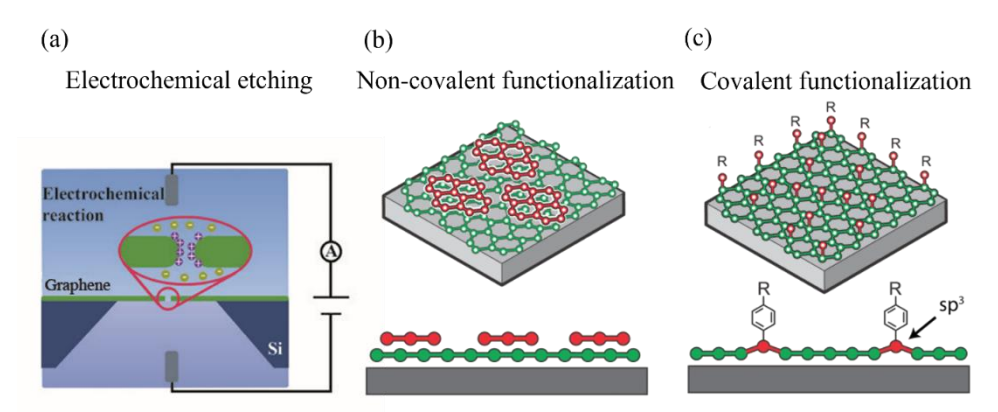


**Figure 13.** (a) Schematic of the electrochemical etching for precise nanopore generation. Adapted from ref<sup>120</sup>. (b) Non-covalent functionalization, where functional groups via  $\pi$ - $\pi$  stacking and van der Waals interactions with the graphene surface. (c) Covalent functionalization, where functional groups are bonded to carbon atoms of the graphene lattice. Adapted from <a href="http://surfchem.dk/research/projects/graphene-chemistry/">http://surfchem.dk/research/projects/graphene-chemistry/</a>.

#### 1.3. Aim and Outline.

Graphene, a single layer of carbon atoms, exhibits exceptional mechanical strength and remarkably low transmembrane resistance. These unique properties make graphene an ideal candidate for applications in ion and molecular sieving. This thesis aims to investigate the potential of monolayer graphene for selective ion sieving, with a focus on proton-metal ion separation. Central to this study is the strategic implementation of surface chemical modification techniques – including covalent functionalization and defect engineering – to systematically enhance ion selectivity.

Chapter 2 presents the preparation of a range of pristine graphene ion transport devices using mechanically exfoliated graphene. Through statistical analysis, we identified key challenges – including contamination, mechanical damage, and interface leakage – that limit device yield. We propose and implement solutions such as transfer protocol optimization, significantly improving device success rates. We identified and examined various factors contributing to device failure and discussed potential solutions to improve the experimental success rate.

Based on our understanding that delamination of graphene is the primary cause of unsuccessful devices, **Chapter 3** uses an adhesion layer based on a pyrene molecule previously developed in the group to enhance the adhesion between graphene and the substrate. This was achieved by increasing the hydrophobicity of the SiN substrate surface and through  $\pi$ - $\pi$  interactions between pyrene and graphene. Incorporating this coating layer significantly improved the scalability of device fabrication and increased the overall success rate.

Chapter 4 discusses the covalent functionalization of graphene (mechanically exfoliated and CVD graphene) using 4-sulfonatobenzene diazonium to create a proton-selective membrane based on graphene. The functionalization process supplemented graphene with sulfonic acid (-SO<sub>3</sub>H) groups, which enhanced the surface hydrophilicity and enabled proton hopping *via* the Grotthuss mechanism. Additionally, sp³-hybridized sites resulting from the disruption of the graphene  $\pi$ -conjugation by the diazotization reaction created additional localized conductive pathways. These modifications enabled proton transport. As a result, the functionalized graphene formed an atomically thin, transmembrane pathway that allowed a more efficient proton conduction compared to pristine graphene while simultaneously blocking the passage of other metal cations. Our findings suggest that the proton permeability of other 2D materials can also be enhanced through similar functionalization strategies. This opens new possibilities for the application of functionalized 2D materials in various hydrogen-related technologies, such as fuel cells, hydrogen storage, and hydrogen separation membranes.

**Chapter 5** describes the enhancement of the monovalent ion selectivity of graphene using a two-step functionalization method. The first step oxidizes the graphene surface with oxygen plasma to introduce active defect sites and increase surface hydrophilicity, facilitating the subsequent reaction with diazonium salts. In the second step, the graphene basal plane and defect sites were modified with 4-sulfonatobenzene diazonium. This synergistic interaction between the surface chemistry and the nanoporous structure resulted in high H<sup>+</sup>/K<sup>+</sup> and K<sup>+</sup>/Cl<sup>-</sup> selectivity ratios, alongside osmotic energy generation.

**Chapter 6** introduces a fabrication technique using a single layer of graphene as a template for nanoskiving to produce nanometer-thick graphene nanoribbons (GNRs) *via* ultramicrotomy. This process requires embedding graphene in a polymeric resin matrix, which can cause mechanical defects during cutting due to the hardness disparity between graphene and the matrix. The study explores the effects of the cutting angles on graphene integrity, aiming to test the electrical properties of the

GNRs and utilize exposed graphene edges for sensing applications. The results show that a 0° cutting angle minimizes stress and produces intact, continuous GNRs with exposed edges, while cutting at 90° and 45° introduces varying damage, with intact-to-fractured ratios of 10:1 and 20:1, respectively. This method provides a simple way to control edge spacing and fabricate width-controlled GNR devices for next-generation electronic technologies.

The overall goal of this PhD thesis was to develop effective graphene-based nanofluidic devices by developing scalable fabrication methods and elucidating proton transport mechanisms. By integrating covalent functionalization, defect engineering, and surface chemistry, we demonstrated the importance of the chemical functionality of graphene in mediating proton transport across its basal plane. The foundational insights into proton hopping mechanisms, interfacial hydrophilicity, and charge-driven ion dynamics are explored with the aim of establishing chemical correlations between the chemical functionality of 2D materials and their membrane properties. Successful realization of these objectives could lead to advancements in energy storage, electronics, and materials science, providing chemical insights into next-generation technologies utilizing 2D materials in membranes.

# 1.4 References.

- [1]. J. Payandeh, T. Scheuer, N. Zheng and W. A. Catterall. The crystal structure of a voltage-gated sodium channel. *Nature* 2011, **475**, 353-358.
- [2]. H. E. Kato, Y. S. Kim, J. M. Paggi, K. E. Evans, W. E. Allen, C. Richardson, K. Inoue, S. Ito, C. Ramakrishnan, L. E. Fenno, K. Yamashita, D. Hilger, S. Y. Lee, A. Berndt, K. Shen, H. Kandori, R. O. Dror, B. K. Kobilka and K. Deisseroth. Structural mechanisms of selectivity and gating in anion channelrhodopsins. *Nature* 2018, 561, 349-354.
- [3]. B. Corry and S. H. Chung. Mechanisms of valence selectivity in biological ion channels. *Cell Mol Life Sci* 2006, **63**, 301-315.
- [4]. E. Gouaux and R. Mackinnon. Principles of selective ion transport in channels and pumps. *Science* 2005, **310**, 1461-1465.
- [5]. B. Corry. The naked truth about K<sup>+</sup> selectivity. *Nat Chem* 2018, **10**, 799-800.
- [6]. R. Epsztein, R. M. DuChanois, C. L. Ritt, A. Noy and M. Elimelech. Towards single-species selectivity of membranes with subnanometre pores. *Nat Nanotechnol* 2020, **15**, 426-436.
- [7]. P. Wang, M. Wang, F. Liu, S. Ding, X. Wang, G. Du, J. Liu, P. Apel, P. Kluth, C. Trautmann and Y. Wang. Ultrafast ion sieving using nanoporous polymeric membranes. *Nat Commun* 2018, **9**, 569.
- [8]. F. Sheng, B. Wu, X. Li, T. Xu, M. A. Shehzad, X. Wang, L. Ge, H. Wang and T. Xu. Efficient ion sieving in covalent organic framework membranes with sub-2-nanometer channels. *Adv Mater* 2021, **33**, e2104404.
- [9]. L. Chen, G. Shi, J. Shen, B. Peng, B. Zhang, Y. Wang, F. Bian, J. Wang, D. Li, Z. Qian, G. Xu, G. Liu, J. Zeng, L. Zhang, Y. Yang, G. Zhou, M. Wu, W. Jin, J. Li and H. Fang. Ion sieving in graphene oxide membranes via cationic control of interlayer spacing. *Nature* 2017, 550, 380-383.
- [10]. V. P. Chauhan, T. Stylianopoulos, Y. Boucher and R. K. Jain. Delivery of molecular and nanoscale medicine to tumors: transport barriers and strategies. *Annu Rev Chem Biomol Eng* 2011, **2**, 281-298.

- [11]. X. Liu, M. Wei, Y. Liu, B. Lv, W. Wei, Y. Zhang and S. Liu. Label-free detection of telomerase activity in urine using telomerase-responsive porous anodic alumina nanochannels. *Anal Chem* 2016, **88**, 8107-8114.
- [12]. X. P. Zhao, Y. Zhou, Q. W. Zhang, D. R. Yang, C. Wang and X. H. Xia. Nanochannel-ion channel hybrid device for ultrasensitive monitoring of biomolecular recognition events. *Anal Chem* 2019, **91**, 1185-1193.
- [13]. K. A. Mauritz and R. B. Moore. State of understanding of Nafion. *Chem Rev* 2004, **104**, 4535-4585.
- [14]. P. Simon and Y. Gogotsi. Materials for electrochemical capacitors. *Nat Mater* 2008, 7, 845-854.
- [15]. Q. Guo, W. Li, X. Li, J. Zhang, D. Sabaghi, J. Zhang, B. Zhang, D. Li, J. Du, X. Chu, S. Chung, K. Cho, N. N. Nguyen, Z. Liao, Z. Zhang, X. Zhang, G. F. Schneider, T. Heine, M. Yu and X. Feng. Proton-selective coating enables fast-kinetics high-mass-loading cathodes for sustainable zinc batteries. *Nat Commun* 2024, 15, 2139.
- [16]. J. R. Werber, C. O. Osuji and M. Elimelech. Materials for next-generation desalination and water purification membranes. *Nat Rev Mater* 2016, 1, 16018.
- [17]. M. A. Shannon, P. W. Bohn, M. Elimelech, J. G. Georgiadis, B. J. Marinas and A. M. Mayes. Science and technology for water purification in the coming decades. *Nature* 2008, **452**, 301-310.
- [18]. M. Elimelech and W. A. Phillip. The future of seawater desalination: energy, technology, and the environment. *Science* 2011, **333**, 712-717.
- [19]. H. Zhang, X. Li, J. Hou, L. Jiang and H. Wang. Angstrom-scale ion channels towards single-ion selectivity. *Chem Soc Rev* 2022, **51**, 2224-2254.
- [20]. X. Yu and W. C. Ren. Ion and Water Transport in 2D Nanofluidic Channels. *Adv Funct Mater* 2024, **34**, 2313968.
- [21]. C. W. Chu, A. R. Fauziah and L. H. Yeh. Optimizing membranes for osmotic power generation. *Angew Chem Int Ed Engl* 2023, **62**, e202303582.

- [22]. M. A. Brown, A. Goel and Z. Abbas. Effect of electrolyte concentration on the Stern layer thickness at a charged interface. *Angew Chem Int Ed Engl* 2016, **55**, 3790-3794.
- [23]. K. Xiao, L. Jiang and M. Antonietti. Ion transport in nanofluidic devices for energy harvesting. *Joule* 2019, **3**, 2364-2380.
- [24]. A. M. Smith, A. A. Lee and S. Perkin. The electrostatic screening length in concentrated electrolytes increases with concentration. *J Phys Chem Lett* 2016, 7, 2157-2163.
- [25]. W. Sparreboom, A. van den Berg and J. C. Eijkel. Principles and applications of nanofluidic transport. *Nat Nanotechnol* 2009, **4**, 713-720.
- [26]. Z. Slouka, S. Senapati and H. C. Chang. Microfluidic systems with ionselective membranes. Annu Rev Anal Chem (Palo Alto Calif) 2014, 7, 317-335.
- [27]. T. Postler, Z. Slouka, M. Svoboda, M. Pribyl and D. Snita. Parametrical studies of electroosmotic transport characteristics in submicrometer channels. *J Colloid Interface Sci* 2008, **320**, 321-332.
- [28]. H. Daiguji. Ion transport in nanofluidic channels. *Chem Soc Rev* 2010, **39**, 901-911.
- [29]. S. Sahu and M. Zwolak. Ionic selectivity and filtration from fragmented dehydration in multilayer graphene nanopores. *Nanoscale* 2017, **9**, 11424-11428.
- [30]. L. A. Richards, A. I. Schafer, B. S. Richards and B. Corry. Quantifying barriers to monovalent anion transport in narrow non-polar pores. *Phys Chem Chem Phys* 2012, **14**, 11633-11638.
- [31]. X. Pang, X. H. Yu, Y. B. He, S. Dong, X. T. Zhao, J. F. Pan, R. N. Zhang and L. F. Liu. Preparation of monovalent cation perm-selective membranes by controlling surface hydration energy barrier. *Sep Purif Technol* 2021, **270**, 118768.
- [32]. B. Tansel, J. Sager, T. Rector, J. Garland, R. F. Strayer, L. Levine, M. Roberts,

- M. Hummerick and J. Bauer. Significance of hydrated radius and hydration shells on ionic permeability during nanofiltration in dead end and cross flow modes. *Separ Purif Technol* 2006, **51**, 40-47.
- [33]. E. R. Nightingale. Phenomenological theory of ion solvation. Effective radii of hydrated ions. *J Phys Chem* 2002, **63**, 1381-1387.
- [34]. Y. Marcus. Thermodynamics of solvation of ions. Part 5. Gibbs free energy of hydration at 298.15 K. *J Chem Soc Faraday Trans* 1991, **87**, 2995-2999.
- [35]. Z. Zhu, D. Wang, Y. Tian and L. Jiang. Ion/molecule transportation in nanopores and nanochannels: from critical principles to diverse functions. *J Am Chem Soc* 2019, **141**, 8658-8669.
- [36]. Z. Zhang, X. Sui, P. Li, G. Xie, X. Y. Kong, K. Xiao, L. Gao, L. Wen and L. Jiang. Ultrathin and ion-selective Janus membranes for high-performance osmotic energy conversion. *J Am Chem Soc* 2017, **139**, 8905-8914.
- [37]. S. Siracusano, V. Baglio, A. Stassi, L. Merlo, E. Moukheiber and A. S. Arico'. Performance analysis of short-side-chain Aquivion® perfluorosulfonic acid polymer for proton exchange membrane water electrolysis. *J Membrane Sci* 2014, **466**, 1-7.
- [38]. R. Fan, S. Huh, R. Yan, J. Arnold and P. Yang. Gated proton transport in aligned mesoporous silica films. *Nat Mater* 2008, 7, 303-307.
- [39]. J. Gao, W. Guo, D. Feng, H. Wang, D. Zhao and L. Jiang. High-performance ionic diode membrane for salinity gradient power generation. *J Am Chem Soc* 2014, **136**, 12265-12272.
- [40]. P. Choi, N. H. Jalani and R. Datta. Thermodynamics and proton transport in Nafion. *J Electrochem Soc* 2005, **152**, E123-E130.
- [41]. D. R. Dreyer, S. Park, C. W. Bielawski and R. S. Ruoff. The chemistry of graphene oxide. *Chem Soc Rev* 2010, **39**, 228-240.
- [42]. R. R. Nair, H. A. Wu, P. N. Jayaram, I. V. Grigorieva and A. K. Geim. Unimpeded permeation of water through helium-leak-tight graphene-based membranes. *Science* 2012, **335**, 442-444.

- [43]. B. Mi. Graphene oxide membranes for ionic and molecular sieving. *Science* 2014, **343**, 740-742.
- [44]. Y. Gogotsi. MXenes-from discovery to applications of two-dimensional metal carbides and nitrides. CRC Press, 2023.
- [45]. B. Anasori, M. R. Lukatskaya and Y. Gogotsi. 2D metal carbides and nitrides (MXenes) for energy storage. *Nat Rev Mater* 2017, **2**, 16098.
- [46]. M. Ghorbani-Asl, N. Zibouche, M. Wahiduzzaman, A. F. Oliveira, A. Kuc and T. Heine. Electromechanics in MoS<sub>2</sub> and WS<sub>2</sub>: nanotubes vs. monolayers. *Sci Rep* 2013, **3**, 2961.
- [47]. M. Chhowalla, Z. Liu and H. Zhang. Two-dimensional transition metal dichalcogenide (TMD) nanosheets. *Chem Soc Rev* 2015, **44**, 2584-2586.
- [48]. B. Liu, Q. Han, L. Li, S. Zheng, Y. Shu, J. A. Pedersen and Z. Wang. Synergistic effect of metal cations and visible light on 2D MoS<sub>2</sub> nanosheet aggregation. *Environ Sci Technol* 2021, **55**, 16379-16389.
- [49]. Z. Wang, Q. Tu, A. Sim, J. Yu, Y. Duan, S. Poon, B. Liu, Q. Han, J. J. Urban, D. Sedlak and B. Mi. Superselective removal of lead from water by two-dimensional MoS<sub>2</sub> nanosheets and layer-stacked membranes. *Environ Sci Technol* 2020, 54, 12602-12611.
- [50]. H. Zhang, J. Hou, Y. Hu, P. Wang, R. Ou, L. Jiang, J. Z. Liu, B. D. Freeman, A. J. Hill and H. Wang. Ultrafast selective transport of alkali metal ions in metal organic frameworks with subnanometer pores. *Sci Adv* 2018, 4, eaaq0066.
- [51]. Y. Peng, Y. Li, Y. Ban, H. Jin, W. Jiao, X. Liu and W. Yang. Metal-organic framework nanosheets as building blocks for molecular sieving membranes. *Science* 2014, **346**, 1356-1359.
- [52]. T. Zhu, Y. Kong, B. Lyu, L. Cao, B. Shi, X. Wang, X. Pang, C. Fan, C. Yang, H. Wu and Z. Jiang. 3D covalent organic framework membrane with fast and selective ion transport. *Nat Commun* 2023, 14, 5926.
- [53]. Z. Wang, Z. Zhang, H. Qi, A. Ortega-Guerrero, L. Wang, K. Xu, M. Wang,

- S. Park, F. Hennersdorf, A. Dianat, A. Croy, H. Komber, G. Cuniberti, J. J. Weigand, U. Kaiser, R. Dong and X. Feng. On-water surface synthesis of charged two-dimensional polymer single crystals via the irreversible Katritzky reaction. *Nat Synth* 2021, **1**, 69-76.
- [54]. X. Feng, X. Ding and D. Jiang. Covalent organic frameworks. *Chem Soc Rev* 2012, 41, 6010-6022.
- [55]. G. Hummer, J. C. Rasaiah and J. P. Noworyta. Water conduction through the hydrophobic channel of a carbon nanotube. *Nature* 2001, **414**, 188-190.
- [56]. J. K. Holt, H. G. Park, Y. Wang, M. Stadermann, A. B. Artyukhin, C. P. Grigoropoulos, A. Noy and O. Bakajin. Fast mass transport through sub-2-nanometer carbon nanotubes. *Science* 2006, **312**, 1034-1037.
- [57]. Y. Li, Z. Li, R. P. Misra, C. Liang, A. J. Gillen, S. Zhao, J. Abdullah, T. Laurence, J. A. Fagan, N. Aluru, D. Blankschtein and A. Noy. Molecular transport enhancement in pure metallic carbon nanotube porins. *Nat Mater* 2024, **23**, 1123-1130.
- [58]. A. Siria, P. Poncharal, A. L. Biance, R. Fulcrand, X. Blase, S. T. Purcell and L. Bocquet. Giant osmotic energy conversion measured in a single transmembrane boron nitride nanotube. *Nature* 2013, **494**, 455-458.
- [59]. F. H. van der Heyden, D. Stein and C. Dekker. Streaming currents in a single nanofluidic channel. *Phys Rev Lett* 2005, **95**, 116104.
- [60]. A. Esfandiar, B. Radha, F. C. Wang, Q. Yang, S. Hu, S. Garaj, R. R. Nair, A. K. Geim and K. Gopinadhan. Size effect in ion transport through angstrom-scale slits. *Science* 2017, **358**, 511-513.
- [61]. A. Bhardwaj, M. V. Surmani Martins, Y. You, R. Sajja, M. Rimmer, S. Goutham, R. Qi, S. Abbas Dar, B. Radha and A. Keerthi. Fabrication of angstrom-scale two-dimensional channels for mass transport. *Nat Protoc* 2024, 19, 240-280.
- [62]. S. P. Surwade, S. N. Smirnov, I. V. Vlassiouk, R. R. Unocic, G. M. Veith, S. Dai and S. M. Mahurin. Water desalination using nanoporous single-layer graphene. *Nat Nanotechnol* 2015, **10**, 459-464.

- [63]. D. E. Jiang, V. R. Cooper and S. Dai. Porous graphene as the ultimate membrane for gas separation. *Nano Lett* 2009, **9**, 4019-4024.
- [64]. H. Du, J. Li, J. Zhang, G. Su, X. Li and Y. Zhao. Separation of hydrogen and nitrogen gases with porous graphene membrane. *J Phys Chem C* 2011, **115**, 23261-23266.
- [65]. J. Schrier. Helium separation using porous graphene membranes. *J Phys Chem Lett* 2010, **1**, 2284-2287.
- [66]. A. W. Hauser and P. Schwerdtfeger. Nanoporous graphene membranes for efficient <sup>3</sup>He/<sup>4</sup>He separation. *J Phys Chem Lett* 2012, **3**, 209-213.
- [67]. S. Blankenburg, M. Bieri, R. Fasel, K. Mullen, C. A. Pignedoli and D. Passerone. Porous graphene as an atmospheric nanofilter. *Small* 2010, **6**, 2266-2271.
- [68]. J. C. Meyer, A. K. Geim, M. I. Katsnelson, K. S. Novoselov, T. J. Booth and S. Roth. The structure of suspended graphene sheets. *Nature* 2007, **446**, 60-63.
- [69]. M. Miao, M. B. Nardelli, Q. Wang and Y. Liu. First principles study of the permeability of graphene to hydrogen atoms. *Phys Chem Chem Phys* 2013, 15, 16132-16137.
- [70]. J. S. Bunch, S. S. Verbridge, J. S. Alden, A. M. van der Zande, J. M. Parpia, H. G. Craighead and P. L. McEuen. Impermeable atomic membranes from graphene sheets. *Nano Lett* 2008, 8, 2458-2462.
- [71]. P. Z. Sun, Q. Yang, W. J. Kuang, Y. V. Stebunov, W. Q. Xiong, J. Yu, R. R. Nair, M. I. Katsnelson, S. J. Yuan, I. V. Grigorieva, M. Lozada-Hidalgo, F. C. Wang and A. K. Geim. Limits on gas impermeability of graphene. *Nature* 2020, 579, 229-232.
- [72]. L. Tsetseris and S. T. Pantelides. Graphene: an impermeable or selectively permeable membrane for atomic species? *Carbon* 2014, **67**, 58-63.
- [73]. S. Hu, M. Lozada-Hidalgo, F. C. Wang, A. Mishchenko, F. Schedin, R. R. Nair, E. W. Hill, D. W. Boukhvalov, M. I. Katsnelson, R. A. Dryfe, I. V.

- Grigorieva, H. A. Wu and A. K. Geim. Proton transport through one-atom-thick crystals. *Nature* 2014, **516**, 227-230.
- [74]. J. L. Achtyl, R. R. Unocic, L. Xu, Y. Cai, M. Raju, W. Zhang, R. L. Sacci, I. V. Vlassiouk, P. F. Fulvio, P. Ganesh, D. J. Wesolowski, S. Dai, A. C. van Duin, M. Neurock and F. M. Geiger. Aqueous proton transfer across single-layer graphene. *Nat Commun* 2015, 6, 6539.
- [75]. F. Banhart, J. Kotakoski and A. V. Krasheninnikov. Structural defects in graphene. *ACS Nano* 2011, **5**, 26-41.
- [76]. Y. An, A. F. Oliveira, T. Brumme, A. Kuc and T. Heine. Stone-Wales defects cause high proton permeability and isotope selectivity of single-layer graphene. *Adv Mater* 2020, **32**, e2002442.
- [77]. E. Griffin, L. Mogg, G. P. Hao, G. Kalon, C. Bacaksiz, G. Lopez-Polin, T. Y. Zhou, V. Guarochico, J. Cai, C. Neumann, A. Winter, M. Mohn, J. H. Lee, J. Lin, U. Kaiser, I. V. Grigorieva, K. Suenaga, B. Ozyilmaz, H. M. Cheng, W. Ren, A. Turchanin, F. M. Peeters, A. K. Geim and M. Lozada-Hidalgo. Proton and Li-ion permeation through graphene with eight-atom-ring defects. ACS Nano 2020, 14, 7280-7286.
- [78]. C. L. Bentley, M. Kang, S. Bukola, S. E. Creager and P. R. Unwin. High-resolution ion-flux imaging of proton transport through graphene|Nafion membranes. *ACS Nano* 2022, **16**, 5233-5245.
- [79]. G. Jayamaha, M. Maleki, C. L. Bentley and M. Kang. Practical guidelines for the use of scanning electrochemical cell microscopy (SECCM). *Analyst* 2024, **149**, 2542-2555.
- [80]. N. Ebejer, M. Schnippering, A. W. Colburn, M. A. Edwards and P. R. Unwin. Localized high resolution electrochemistry and multifunctional imaging: scanning electrochemical cell microscopy. *Anal Chem* 2010, **82**, 9141-9145.
- [81]. M. Bartolomei, M. I. Hernández, J. Campos-Martínez and R. Hernández-Lamoneda. Graphene multi-protonation: a cooperative mechanism for proton permeation. *Carbon* 2019, **144**, 724-730.
- [82]. Y. Feng, J. Chen, W. Fang, E. G. Wang, A. Michaelides and X. Z. Li.

- Hydrogenation facilitates proton transfer through two-dimensional honeycomb crystals. *J Phys Chem Lett* 2017, **8**, 6009-6014.
- [83]. W. L. Wang and E. Kaxiras. Graphene hydrate: theoretical prediction of a new insulating form of graphene. *New J Phys* 2010, **12**, 125012.
- [84]. I. Poltavsky, L. Zheng, M. Mortazavi and A. Tkatchenko. Quantum tunneling of thermal protons through pristine graphene. *J Chem Phys* 2018, **148**, 204707.
- [85]. J. Tong, Y. Fu, D. Domaretskiy, F. Della Pia, P. Dagar, L. Powell, D. Bahamon, S. Huang, B. Xin, R. N. Costa Filho, L. F. Vega, I. V. Grigorieva, F. M. Peeters, A. Michaelides and M. Lozada-Hidalgo. Control of proton transport and hydrogenation in double-gated graphene. *Nature* 2024, 630, 619-624.
- [86]. O. J. Wahab, E. Daviddi, B. Xin, P. Z. Sun, E. Griffin, A. W. Colburn, D. Barry, M. Yagmurcukardes, F. M. Peeters, A. K. Geim, M. Lozada-Hidalgo and P. R. Unwin. Proton transport through nanoscale corrugations in two-dimensional crystals. *Nature* 2023, 620, 782-786.
- [87]. Y.-A. Li, H. Hu, W. Xu and Y.-G. Zhou. Nanoripples in graphene: a remarkable structure for proton mass transport. *Innov Mater* 2024, **2**, 100053.
- [88]. Jan Stehr, Irina Buyanova and W. Chen. Structural defects in graphene, defects in advanced electronic materials and novel low dimensional structures. Matthew Deans, 2018.
- [89]. S. K. Tiwari, S. K. Pandey, R. Pandey, N. Wang, M. Bystrzejewski, Y. K. Mishra and Y. Zhu. Stone-Wales defect in graphene. *Small* 2023, **19**, e2303340.
- [90]. G. D. Lee, C. Z. Wang, E. Yoon, N. M. Hwang, D. Y. Kim and K. M. Ho. Diffusion, coalescence, and reconstruction of vacancy defects in graphene layers. *Phys Rev Lett* 2005, **95**, 205501.
- [91]. A. J. Stone and D. J. Wales. Theoretical studies of icosahedral C60 and some related species. *Chem Phys Lett* 1986, **128**, 501-503.

- [92]. O. V. Yazyev and S. G. Louie. Topological defects in graphene: dislocations and grain boundaries. *Phys Rev B* 2010, **81**, 195420.
- [93]. B. W. Jeong, J. Ihm and G.-D. Lee. Stability of dislocation defect with two pentagon-heptagon pairs in graphene. *Phys Rev B* 2008, **78**, 165403.
- [94]. K. S. Kim, Y. Zhao, H. Jang, S. Y. Lee, J. M. Kim, K. S. Kim, J. H. Ahn, P. Kim, J. Y. Choi and B. H. Hong. Large-scale pattern growth of graphene films for stretchable transparent electrodes. *Nature* 2009, **457**, 706-710.
- [95]. P. Y. Huang, C. S. Ruiz-Vargas, A. M. van der Zande, W. S. Whitney, M. P. Levendorf, J. W. Kevek, S. Garg, J. S. Alden, C. J. Hustedt, Y. Zhu, J. Park, P. L. McEuen and D. A. Muller. Grains and grain boundaries in single-layer graphene atomic patchwork quilts. *Nature* 2011, 469, 389-392.
- [96]. J. Lahiri, Y. Lin, P. Bozkurt, Oleynik, II and M. Batzill. An extended defect in graphene as a metallic wire. *Nat Nanotechnol* 2010, **5**, 326-329.
- [97]. G. H. Lee, R. C. Cooper, S. J. An, S. Lee, A. van der Zande, N. Petrone, A. G. Hammerberg, C. Lee, B. Crawford, W. Oliver, J. W. Kysar and J. Hone. High-strength chemical-vapor-deposited graphene and grain boundaries. *Science* 2013, 340, 1073-1076.
- [98]. L. P. Biró and P. Lambin. Grain boundaries in graphene grown by chemical vapor deposition. *New J Phys* 2013, **15**, 035024.
- [99]. A. W. Tsen, L. Brown, R. W. Havener and J. Park. Polycrystallinity and stacking in CVD graphene. *Acc Chem Res* 2013, **46**, 2286-2296.
- [100]. C. T. Toh, H. Zhang, J. Lin, A. S. Mayorov, Y. P. Wang, C. M. Orofeo, D. B. Ferry, H. Andersen, N. Kakenov, Z. Guo, I. H. Abidi, H. Sims, K. Suenaga, S. T. Pantelides and B. Ozyilmaz. Synthesis and properties of free-standing monolayer amorphous carbon. *Nature* 2020, 577, 199-203.
- [101]. C. Zhang, L. Fu, N. Liu, M. Liu, Y. Wang and Z. Liu. Synthesis of nitrogen-doped graphene using embedded carbon and nitrogen sources. *Adv Mater* 2011, **23**, 1020-1024.
- [102]. K. Yan, L. Fu, H. Peng and Z. Liu. Designed CVD growth of graphene via

- process engineering. Acc Chem Res 2013, 46, 2263-2274.
- [103]. J. Wang, C. Cheng, X. Zheng, J. C. Idrobo, A. Y. Lu, J. H. Park, B. G. Shin, S. J. Jung, T. Zhang, H. Wang, G. Gao, B. Shin, X. Jin, L. Ju, Y. Han, L. J. Li, R. Karnik and J. Kong. Cascaded compression of size distribution of nanopores in monolayer graphene. *Nature* 2023, 623, 956-963.
- [104]. A. V. Krasheninnikov and F. Banhart. Engineering of nanostructured carbon materials with electron or ion beams. *Nat Mater* 2007, **6**, 723-733.
- [105]. L. Liu, M. Qing, Y. Wang and S. Chen. Defects in graphene: generation, healing, and their effects on the properties of graphene: a review. *J Mater Sci Technol* 2015, **31**, 599-606.
- [106]. D. Teweldebrhan and A. A. Balandin. Modification of graphene properties due to electron-beam irradiation. *Appl Phys Lett* 2009, **94**, 013101.
- [107]. K. Yoon, A. Rahnamoun, J. L. Swett, V. Iberi, D. A. Cullen, I. V. Vlassiouk, A. Belianinov, S. Jesse, X. Sang, O. S. Ovchinnikova, A. J. Rondinone, R. R. Unocic and A. C. van Duin. Atomistic-scale simulations of defect formation in graphene under noble gas ion irradiation. ACS Nano 2016, 10, 8376-8384.
- [108]. G. Compagnini, F. Giannazzo, S. Sonde, V. Raineri and E. Rimini. Ion irradiation and defect formation in single layer graphene. *Carbon* 2009, **47**, 3201-3207.
- [109]. O. Lehtinen, J. Kotakoski, A. V. Krasheninnikov and J. Keinonen. Cutting and controlled modification of graphene with ion beams. *Nanotechnology* 2011, **22**, 175306.
- [110]. C. J. Russo and J. A. Golovchenko. Atom-by-atom nucleation and growth of graphene nanopores. *Proc Natl Acad Sci U S A* 2012, **109**, 5953-5957.
- [111]. S. C. O'Hern, M. S. Boutilier, J. C. Idrobo, Y. Song, J. Kong, T. Laoui, M. Atieh and R. Karnik. Selective ionic transport through tunable subnanometer pores in single-layer graphene membranes. *Nano Lett* 2014, **14**, 1234-1241.
- [112]. H. Qi, Z. Li, Y. Tao, W. Zhao, K. Lin, Z. Ni, C. Jin, Y. Zhang, K. Bi and Y.

- Chen. Fabrication of sub-nanometer pores on graphene membrane for ion selective transport. *Nanoscale* 2018, **10**, 5350-5357.
- [113]. P. Chaturvedi, I. V. Vlassiouk, D. A. Cullen, A. J. Rondinone, N. V. Lavrik and S. N. Smirnov. Ionic conductance through graphene: assessing its applicability as a proton selective membrane. *ACS Nano* 2019, **13**, 12109-12119.
- [114]. Y. Yamada, K. Murota, R. Fujita, J. Kim, A. Watanabe, M. Nakamura, S. Sato, K. Hata, P. Ercius, J. Ciston, C. Y. Song, K. Kim, W. Regan, W. Gannett and A. Zettl. Subnanometer vacancy defects introduced on graphene by oxygen gas. *J Am Chem Soc* 2014, **136**, 2232-2235.
- [115]. X. Zhang, P. M. G. van Deursen, W. Fu and G. F. Schneider. Facile and ultraclean graphene-on-glass nanopores by controlled electrochemical etching. *ACS Sens* 2020, **5**, 2317-2325.
- [116]. J. Feng, K. Liu, M. Graf, M. Lihter, R. D. Bulushev, D. Dumcenco, D. T. Alexander, D. Krasnozhon, T. Vuletic, A. Kis and A. Radenovic. Electrochemical reaction in single layer MoS<sub>2</sub>: nanopores opened atom by atom. *Nano Lett* 2015, **15**, 3431-3438.
- [117]. S. E. Wheeler. Understanding substituent effects in noncovalent interactions involving aromatic rings. *Acc Chem Res* 2013, **46**, 1029-1038.
- [118]. J. Park and M. Yan. Covalent functionalization of graphene with reactive intermediates. *Acc Chem Res* 2013, **46**, 181-189.
- [119]. G. L. Paulus, Q. H. Wang and M. S. Strano. Covalent electron transfer chemistry of graphene with diazonium salts. *Acc Chem Res* 2013, **46**, 160-170.
- [120]. W. Zhang. Functionalizing monolayer graphene as a proton-selective membrane for direct methanol fuel cells. PhD thesis, 2023.